International Journal of Nanomedicine Dovepress

Open Access Full Text Article ORIGINAL RESEARCH

Near-Infrared Driven Gold Nanoparticles-Decorated g-C_3N_4/SnS_2 Heterostructure through Photodynamic and Photothermal Therapy for Cancer Treatment

Pranjyan Dash[1], Senthilkumar Thirumurugan[1], Nandini Nataraj[1], Yu-Chien Lin[1–3], Xinke Liu[4,5], Udesh Dhawan[6], Ren-Jei Chung[1,7]

[1]Department of Chemical Engineering and Biotechnology, National Taipei University of Technology (Taipei Tech), Taipei, 10608, Taiwan; [2]School of Materials Science and Engineering, Nanyang Technological University, Singapore, 639798, Singapore; [3]ZhongSun Co., LTD, New Taipei City, 220031, Taiwan; [4]College of Materials Science and Engineering, Chinese Engineering and Research Institute of Microelectronics, Shenzhen University, Shenzhen, 518060, People's Republic of China; [5]Department of Electrical and Computer Engineering, National University of Singapore, Singapore, 117583, Singapore; [6]Centre for the Cellular Microenvironment, Division of Biomedical Engineering, James Watt School of Engineering, Mazumdar-Shaw Advanced Research Centre, University of Glasgow, Glasgow, G116EW, UK; [7]High-Value Biomaterials Research and Commercialization Center, National Taipei University of Technology (Taipei Tech), Taipei, 10608, Taiwan

Correspondence: Ren-Jei Chung, Department of Chemical Engineering and Biotechnology, National Taipei University of Technology (Taipei Tech), No. 1, Sec. 3, Zhongxiao E. Road, Taipei, 10608, Taiwan, Tel +886-2-2771-2171 ext. 2547, Email rjchung@ntut.edu.tw

Background: Phototherapy based on photocatalytic semiconductor nanomaterials has received considerable attention for the cancer treatment. Nonetheless, intense efficacy for in vivo treatment is restricted by inadequate photocatalytic activity and visible light response.

Methods: In this study, we designed a photocatalytic heterostructure using graphitic carbon nitride (g-C_3N_4) and tin disulfide (SnS_2) to synthesize g-C_3N_4/SnS_2 heterostructure through hydrothermal process. Furthermore, Au nanoparticles were decorated in situ deposition on the surface of the g-C_3N_4/SnS_2 heterostructure to form g-C_3N_4/SnS_2@Au nanoparticles.

Results: The g-C_3N_4/SnS_2@Au nanoparticles generated intense reactive oxygen species radicals under near-infrared (NIR) laser irradiation through photodynamic therapy (PDT) pathways (Type-I and Type-II). These nanoparticles exhibited enhanced photothermal therapy (PTT) efficacy with high photothermal conversion efficiency (41%) when subjected to 808 nm laser light, owing to the presence of Au nanoparticles. The in vitro studies have indicated that these nanoparticles can induce human liver carcinoma cancer cell (HepG2) apoptosis (approximately 80% cell death) through the synergistic therapeutic effects of PDT and PTT. The in vivo results demonstrated that these nanoparticles exhibited enhanced efficient antitumor effects based on the combined effects of PDT and PTT.

Conclusion: The g-C_3N_4/SnS_2@Au nanoparticles possessed enhanced photothermal properties and PDT effect, good biocompatibility and intense antitumor efficacy. Therefore, these nanoparticles could be considered promising candidates through synergistic PDT/PTT effects upon irradiation with NIR laser for cancer treatment.

Keywords: g-C_3N_4, SnS_2, Gold nanoparticles, Photodynamic therapy, Photothermal therapy

Introduction

Recently, cancer is the preeminent cause of mortality worldwide.[1,2] Several strategies have been implemented to treat cancer. Photodynamic therapy (PDT) has garnered widespread attention owing to its various advantages, including good applicability, high selectivity, non-invasiveness, intense repeatability, and low toxicity.[3–9] When exposed to light irradiation, a specific photosensitizer (PS) can produce cytotoxic reactive oxygen species (ROS) that lead to cellular apoptosis (destruction of DNA and protein).[10–13] PSs react with biological molecules of substrates that may interact with triplet oxygen ($^3O_2$) or H_2O in Type-I PDT, resulting in the production of $O_2^{-\cdot}$ and $OH^{\cdot}$ radicals.[14] Moreover, PSs can

Received: 14 July 2024
Accepted: 1 October 2024
Published: 17 October 2024

initiate a Type-II PDT pathway to release $^1O_2$ by directly transferring energy to $^3O_2$. The combined Type-I and II PDT pathways have attracted considerable attention for clinical applications. Photothermal therapy (PTT) converts near-infrared (NIR) light energy into hyperthermia at the tumor site, resulting in tumor ablation.[15,16] PTT has attracted considerable interest in cancer therapy owing to its high photothermal stability, spatial and temporal resolution, enhanced conversion efficiency, minimal invasiveness, high selectivity, good biocompatibility, and non-toxicity.[17–24] Heat generation in localized tissues through PTT can boost blood flow for improved O_2 delivery, resulting in a synergistic effect with PDT. The synergistic strategies of PDT and PTT have enormous potential in cancer treatment to improve therapeutic efficiency and overcome complications.[4]

Photocatalytic therapies have garnered considerable interest owing to their favorable chemical and physical functions, strong light absorption, distinct structures, and promotion of photoinduced electron-hole pair separations.[25–27] The design of semiconductor heterostructure photocatalytic materials can improve the photocatalytic efficiency with enhanced electron-hole pair separation under light irradiation, which has received attention for cancer treatment. Graphitic carbon nitride (g-C_3N_4) is a two-dimensional (2D) semiconductor material with various advantages, including enhanced chemical and thermal stability, a unique layered structure, high specific surface area, low cost, low toxicity, good biocompatibility, and intense photocatalytic activity.[28–32] It possesses a moderate band gap (2.7 eV) that can respond to the ultraviolet (UV) and visible regions and has a stronger reduction ability to generate ROS with the activation of molecular oxygen.[33] Furthermore, g-C_3N_4 nanosheets (NSs) can act as PSs to inhibit cancer cells, leading to an improved PDT.[34,35] However, g-C_3N_4 NSs have a fast recombination rate of photoexcited charge carriers and low photon absorption ability, which hinder their application.[28,29,36,37] The manufacturing of g-C_3N_4-based heterostructure nanocomposites using metal oxides, noble metal nanoparticles, and semiconductor materials is an effective strategy that can improve photogenerated charge carrier separation, inhibit the recombination rate, and enhance light absorption efficiency.[28,36] Tin disulfide (SnS_2) is a n-type semiconductor with a band gap of 2.1–2.4 eV and has been extensively studied in various applications including sensors, batteries, photocatalysis, and optoelectronics owing to its improved surface-to-volume ratio, non-toxicity, chemical stability, low cost, and good photocatalytic reduction activity.[29,36,38–42] Furthermore, SnS_2 NSs exhibit enhanced photocatalytic performance and good biocompatibility, and can be utilized for biological applications.[40] SnS_2 can be utilized as an NIR-activated material because of its slight absorption of NIR light and its photothermal activity.[43,44] The incorporation of 2D heterojunctions with g-C_3N_4 materials enhances the charge carrier separation, which improves the photocatalytic activity and increases the efficiency of light absorption.

Plasmonic nanomaterials, particularly Au nanoparticles accompanied by semiconductor nanostructures, have attracted considerable attention for biomedical applications owing to their intense NIR light absorption, good biocompatibility, enhanced physiochemical properties, catalytic activities improved photothermal performance, controlled reduction, facile synthesis controllable changing morphology, shape size, excellent bioimaging, drug delivery, and strong localized surface plasmon resonance effects.[5,45–48] The integration of plasmonic and semiconductor-based nanostructures acts as an electron mediator that can intensify the interfacial electron transfer from the adjacent heterojunction semiconductor materials of the conduction band, promote the separation of electron-hole pairs, enhance photocatalytic activity, and improve light absorption in the NIR region.[49,50] Moreover, combined plasmonic metal and semiconductor heterostructure nanomaterials can promote PDT and PTT effects, which can induce cell apoptosis in cancer treatment. The combination of semiconductor heterostructure nanomaterials and plasmonic metal has limited investigation for cancer treatment.

Zhang et al[28] designed Ti_3C_2/g-C_3N_4 heterostructure with modification of triphenylphosphonium bromide (TPP) to form Ti_3C_2/g-C_3N_4-TPP NSs, which exhibited intense PDT and PTT effects under the NIR light irradiation. Yang et al fabricated Bi_2Se_3/Au (BS/Au) heterostructure, and these heterostructure was later modified using poly (ethylene glycol) methyl ether-block-poly (lactide-co-glycolide) (PLGA-PEG) for improved solubility and biocompatibility.[10] Finally, doxorubicin (DOX) was loaded onto the BS/Au@PLGA-PEG to generate BS/Au@PP-DOX. These nanocomposites enhanced the multimodal synergistic effects of PTT and chemotherapy in cancer treatment.

Herein, we designed a 2D heterostructure (g-C_3N_4/SnS_2), in which the surface was decorated with Au nanoparticles to generate g-C_3N_4/SnS_2@Au nanoparticles. The synthesized nanoparticles PDT and PPT effects was explored under NIR laser irradiation in details. Moreover, nanoparticle's biocompatibility, cytotoxicity, and antitumor efficacy have been extensively discussed through both In vitro and in vivo investigations. The synthesized nanoparticles can be considered

promising candidates for cancer treatment through synergistic therapeutic effects with NIR laser irradiation. The schematic representation of g-C_3N_4/SnS_2@Au nanoparticles with synergistic PDT/PTT effects for the cancer treatment is shown in Scheme 1.

Materials and Methods

The materials information, and characterizations details are available in the Supplementary Information.

Synthesis of g-C_3N_4 Nanosheets

Urea (30 g) was placed in a sealed alumina crucible and calcinated to 550°C (4 h) under muffle furnace. The resultant yellow solid powder was then heated to 500°C (2 h) in order to generate g-C_3N_4 nanosheets.

Synthesis of g-C_3N_4/SnS_2

g-C_3N_4/SnS_2 was synthesized via hydrothermal process. Briefly, $SnCl_4.5H_2O$ (2.2 g) and TAA (0.88 g) was added into deionized (DI) water (80 mL). After that, the aforementioned solution was supplemented with the appropriate quantity of g-C_3N_4. The solution was stirred for 15 min. Then mixture solution was transferred into the autoclave and heated (180°C, 24 h), then cool down at ambient temperature. Then the obtained precipitated was centrifuged, rinsed with DI and ethanol for various times. Lastly, the resulting yellow precipitated was dried (80°C, 12 h).

Synthesis of g-C_3N_4/SnS_2@Au Nanoparticles

The synthesized g-C_3N_4/SnS_2 (30 mg) was suspended in 30 mL DI water and then agitated for 30 min. Subsequently, Au nano seeds (300 µL) were added above into the solution, and gently stirred. The 10 mM $HAuCl_4$ solution and sodium citrate (0.04 M) were added into the aforementioned mixture solution while constant stirring. Subsequently, ascorbic acid (0.1 M) was mixed, and the solution was reacted for 30 min. The resulting precipitated solution was centrifuged and rinsed with DI water. Lastly, the g-C_3N_4/SnS_2@Au nanoparticles were dried at 60°C in the oven overnight.

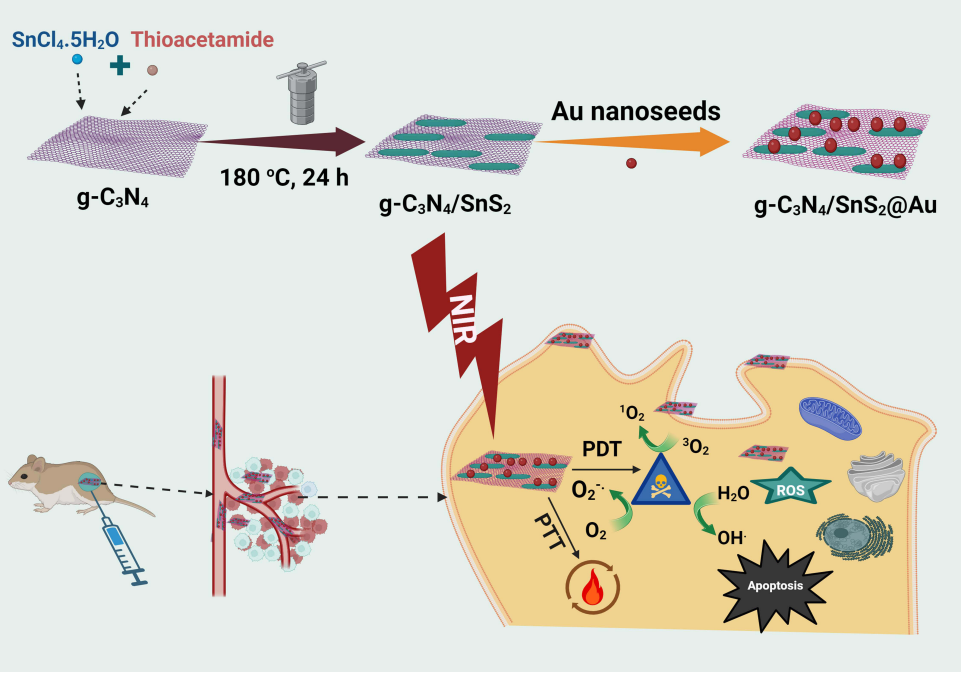

Scheme 1 Schematic diagram for synthesis of g-C_3N_4/SnS_2@Au nanoparticles and its synergistic PDT/PTT effects for cancer therapeutics.

Photothermal Effect of Nanoparticles

The photothermal effect of g-C_3N_4/SnS_2@Au nanoparticles was evaluated at various concentrations by irradiation of NIR laser (1 W/cm^2, 10 min). The photothermal stability was investigated over three rounds of turning the laser on and off, and the nanocomposites' temperature fluctuations were measured. The aqueous nanoparticles (1 mg/mL) were subjected under 808 nm laser for 600 s to determine their photothermal conversion efficiency (η). Afterwards, the laser was switched off, allowed to cool down at ambient temperature. The "η" for nanoparticles was determined from our previous studies.[5]

Extracellular ROS Generation

The g-C_3N_4/SnS_2@Au nanoparticles were immersed with methylene blue (MB) solution (10 µg/mL) and IPA. The sample was exposed to 808 nm laser light at several time durations of 0, 10, 20, and 30 min. The OH. was detected at 664 nm wavelength by UV-Vis spectroscopy. The DPBF as a ROS probe was used for the detection of $^1O_2$ generation. Firstly, stock solution DPBF (0.5 mg/mL) in DMSO was prepared. Consequently, an aqueous solution of g-C_3N_4/SnS_2@Au (1 mg/mL) was mixed into the DPBF solution followed by ultrasonication treatment. This reaction was carried out in dark conditions. The mixture solution was subjected to an NIR laser at different time intervals. Finally, the samples' absorbance was calculated at 410 nm wavelength using UV-Vis spectroscopy. For the detection of extracellular ROS, the DCFH-DA ROS probe was employed. The DCFH-DA (0.5 mL, 1 mM) solution was dissolved methanol and mixed thoroughly. The aforementioned mixture solution was then mixed with 10 mM NaOH solution, followed by stirring for 30 min in dark atmosphere. Subsequently, PBS (pH = 7.4, 10 mM) was added to the mixture to make it neutral. The aforementioned DCFH-DA solution was immersed with g-C_3N_4/SnS_2@Au nanoparticle solution (1 mg/mL). The mixture solution was subjected to NIR laser for different time intervals (0, 5, and 10 min), respectively. The samples fluorescence intensity at 426 nm wavelength was collected through photoluminescence spectra.

Cytotoxicity Studies

Normal fibroblast (L929) and human liver carcinoma cancer (HepG2) cell lines were cultivated in a 96-well plate (24 h). After that, several concentrations of nanoparticles were added. The cells were subjected under 808 nm laser (1 W/cm^2, 5 min). Cell cytotoxicity in HepG2 was examined using the Cell Counting Kit-8 (CCK-8) test. The absorbance of cells was calculated at 450 nm wavelength by an ELISA (Thermo fisher scientific, Finland) reader. The cell lines used in this study were purchased from ATCC cell bank.

Cellular Uptake Analysis

The cellular uptake analysis of g-C_3N_4/SnS_2@Au nanoparticles was performed using inductively coupled plasma-mass-spectrometry (ICP-MS). HepG2 cells (3×10^5) were seeded in a 35 mm culture petri dishes and incubated at 37°C for 24 h. Then culture medium was changed and the cells were washed with PBS. Subsequently, the g-C_3N_4/SnS_2@Au nanoparticles were added inside the cell solution. Further, the cells with nanoparticles were incubated for 1 and 4 h. After incubation, the cells were further treated with hydrochloric acid. Then cellular uptake analysis was performed g-C_3N_4/SnS_2@Au nanoparticles in the cells were determined using ICP-MS.

In vitro Detection of ROS

A ROS probe, DCFH-DA was used to identify the intracellular ROS, which quickly oxidized to DCF products. HepG2 cells (3×10^5) were grown overnight in a culture dish. The g-C_3N_4/SnS_2@Au (250 µg/mL) nanoparticles were added after the medium was aspirated, and PBS was used to wash cells. The cells were stained with nuclei marker 4',6-diamidino-2-phenylindole (DAPI, 10 µM). Furthermore, the dish was incubated (30 min) after the addition of 10 µM of DCFH-DA. The NIR laser was subjected to the cell solution. Fluorescence microscopy was used to detect ROS.

Animal Experiment

HepG2 cells (2×10^6) were subcutaneously injected into Balb/c mice (4-week-old). Afterwards, the growing tumors were separated into three groups: control, g-C_3N_4/SnS_2@Au (250 μg/mL, 100 μL), and g-C_3N_4/SnS_2@Au nanoparticles (250 μg/mL, 100 μL) irradiated under 808 nm laser (0.75 W/cm^2) for 10 min. Tumor volume and body weight were recorded throughout the treatment periods. The following equation was used to determine the tumor volumes was as follows: Tumor volume $V = \frac{LW^2}{2}$, where "L" denotes tumor's length, and "W" stands as the width of the tumor. The mice were euthanized after 14 days of treatment. Their major organs, such as the heart, lungs, kidneys, liver, and spleen, as well as tumors were accumulated and immersed in formalin. Hematoxylin and eosin (H&E) were used to stain tissue slices for histological analysis. All animal experiments were conducted according to the protocols and approval of the Institutional Animal Care and Use Committee of Taipei Medical University (TMU) (document number: LAC2022-0445).

Statistical Analysis

The SPSS software 18.0 (Chicago, USA) was used to do the statistical calculations for all the experimental data. For statistical significance, $p<0.05$ is denoted by the notation "*".

Results and Discussion

Characterization of g-C_3N_4/SnS_2@Au Nanoparticles

The transmission electron microscopy (TEM) images of the g-C_3N_4, g-C_3N_4/SnS_2 and g-C_3N_4/SnS_2@Au nanoparticles are presented in Figure 1A–C. g-C_3N_4 clearly appeared as a 2D sheet structure (Figure 1A). SnS_2 was uniformly attached to the g-C_3N_4 surface (Figure 1B). The average particle size of SnS_2 was approximately calculated as 8 nm. The growth of SnS_2 was shown as a sheet and an ellipsoid-shaped structure that covered the g-C_3N_4 surface. The different morphologies of SnS_2 may depend on the solvent used, which plays an important role in controlling the morphology of SnS_2.[39] Au nanoparticles were then coated onto the surface of g-C_3N_4/SnS_2 (Figure 1C). The Au nanoparticles appeared spherical in shape with average particle size about 15 nm (Figure S1). The high-resolution TEM (HRTEM) images of g-C_3N_4/SnS_2@Au are shown in Figure S2, and the lattice d-spacing of SnS_2 assigned to the (100) and (101) planes was approximately 0.28 and 0.315 nm, respectively. Moreover, the d-spacing of the Au nanoparticles was 0.24

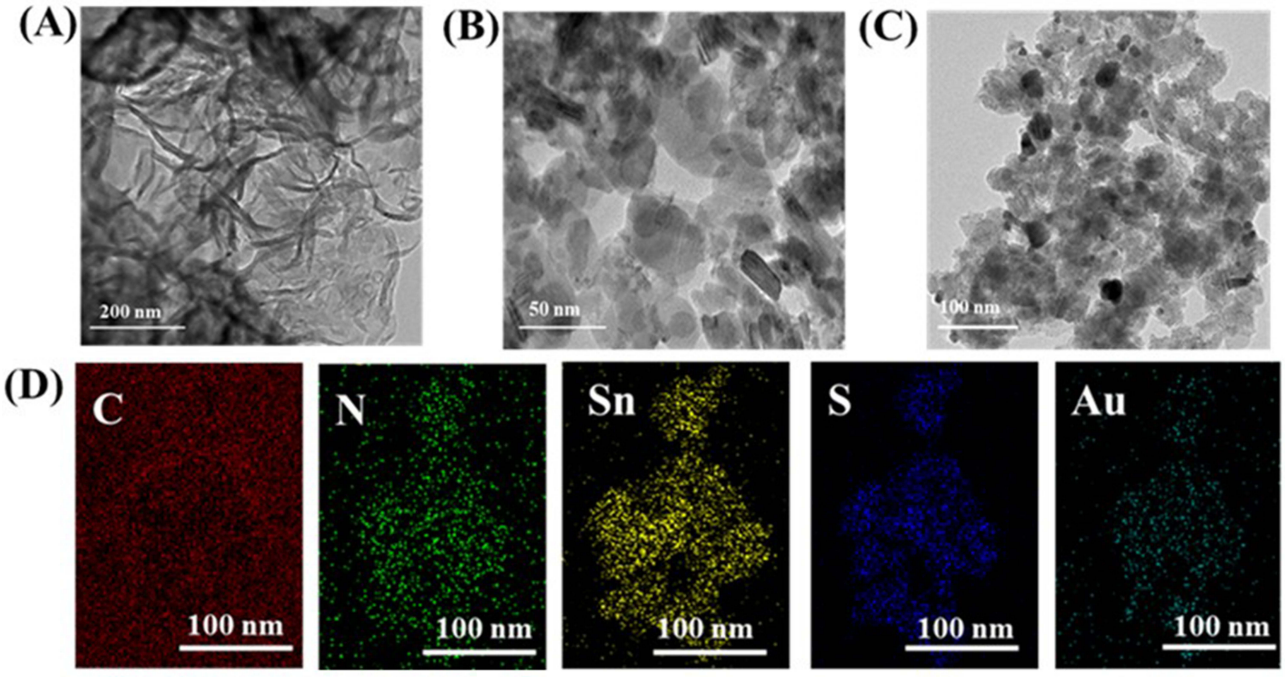

Figure 1 TEM images of (**A**) g-C_3N_4. (**B**) g-C_3N_4/SnS_2. (**C**) g-C_3N_4/SnS_2@Au nanoparticles. (**D**) EDS mapping of g-C_3N_4/SnS_2@Au nanoparticles.

nm, which corresponded to the (111) crystal plane (Figure S2). The EDS mapping in Figure 1D shows the presence of C, N, Sn, S, and Au without any impurities, indicating the successful synthesis of g-C_3N_4/SnS_2@Au nanoparticles.

The crystalline structure of samples was evaluated using X-ray diffraction (XRD) patterns and the results are presented in Figure S3. Two diffraction peaks appeared at 13.06° and 27.75° which correspond to the characteristic planes (100) and (002) of g-C_3N_4.[27] The diffraction peaks at 15.11°, 28.37°, 32.49°, 46.44°, 50.01°, 55.86°, 58.79°, 59.80 °, 63.43 °, and 70.55 ° corresponded to (001), (100), (101), (102), (110), (111), (200), (201), (202), and (113) planes of SnS_2 (JCPDS No. 23–0677). The deposition of Au nanoparticles appeared at 2θ angles of 38.27°, 44.41°, 64.59° and 78.33 ° which attributed to crystal planes (111), (200), (220) and (311), respectively, indicating the face-centered cubic structure (JCPDS No. 04–0783). This suggests that the Au nanoparticles were successfully deposited onto g-C_3N_4/SnS_2. The g-C_3N_4 and SnS_2 diffraction peaks well matched with their standard patterns. These results indicate the successful synthesis of g-C_3N_4/SnS_2@Au nanoparticles. Further chemical structures of all the samples were identified by Fourier-transform infrared spectroscopy (FTIR), as presented in Figure 2A. The absorption band at 3000–3400 cm^{-1} was attributed to the stretching vibration of the N-H group bound to the O-H group, the characteristic peaks at 1634 and 1545 cm^{-1} were attributed to the C=N stretching vibration, and the characteristic peaks at 1407, 1318, and 1233 cm^{-1} were ascribed to the C-N stretching vibration modes of g-C_3N_4. Furthermore, the peaks at 811 cm^{-1} corresponded to the s-triazine ring modes.[36] The absorption peak at 591 cm^{-1} was attributed to Sn-S bond of SnS_2. The remaining characteristic peaks did not alter for g-C_3N_4/SnS_2, which indicated the growth of SnS_2 on g-C_3N_4. For the g-C_3N_4/SnS_2@Au nanoparticles, no extra vibrational peaks appeared for the Au-O bond because the Au-O vibrational peak overlapped with the out-of-plane bending modes of the CN heterocycles.[37] Moreover, the peaks at 812 cm^{-1} had reduced intensity as compared to g-C_3N_4/SnS_2 which confirmed the presence of Au nanoparticles on the surface of g-C_3N_4/SnS_2. A slight shift in peak was observed at 3151 cm^{-1} for g-C_3N_4/SnS_2@Au nanoparticles, which attributed to N-H stretching vibration with O-H bond. However, the other peaks did not change for the g-C_3N_4/SnS_2@Au nanoparticles, indicating the successful fabrication of g-C_3N_4/SnS_2@Au nanoparticles. The UV spectra of all samples are presented in Figure 2B. Pure g-C_3N_4 and SnS_2 exhibited strong absorption at 450 and 550 nm, respectively. The corresponding band gaps of

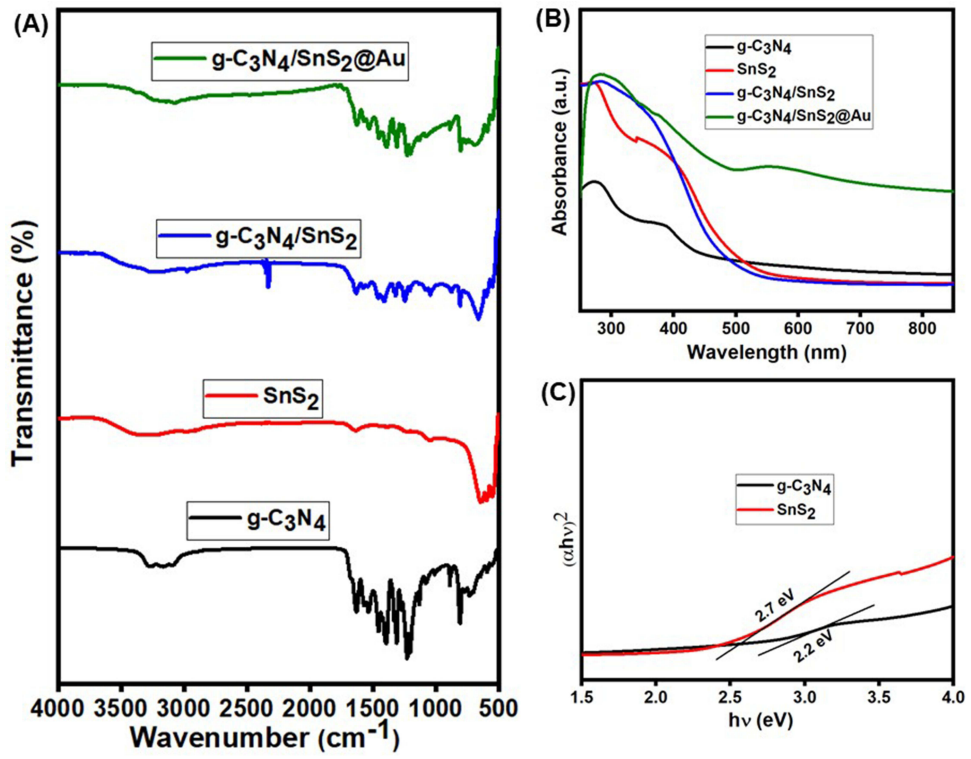

Figure 2 (**A**) FTIR spectra of g-C_3N_4, SnS_2, g-C_3N_4/SnS_2, and g-C_3N_4/SnS_2@Au nanoparticles. (**B**) UV-Vis-NIR absorption spectra of g-C_3N_4, SnS_2, g-C_3N_4/SnS_2, and g-C_3N_4/SnS_2@Au nanoparticles. (**C**) The corresponding band gap of g-C_3N_4 and SnS_2.

g-C_3N_4 and SnS_2 were evaluated and its value were 2.7 eV and 2.1 eV, respectively, as presented in Figure 2C. g-C_3N_4/SnS_2 exhibits a strong absorption peak intensity due owing to the hybridization of g-C_3N_4 and SnS_2.[39] Moreover, after decoration with Au nanoparticles, the g-C_3N_4/SnS_2@Au nanoparticles exhibited a broad NIR light absorption region with increased absorption peak intensity, which could enhance cancer therapeutic treatment. These nanoparticles could be considered as a promising photothermal therapeutic agent and displayed improve photocatalytic activity by signifying charge carrier separation.

The chemical compositions and valence states of the g-C_3N_4/SnS_2@Au nanoparticles were investigated using X-ray photoelectron spectroscopy (XPS) (Figure 3). The C 1s spectrum showed two peaks at 284.2 and 287.5 eV which were attributed to SP^2 hybridized C-C bond and N-C=N bonds of g-C_3N_4, respectively (Figure 3A). The N 1s spectra exhibited four distinct peaks at 398.9, 399.91, 400.1, and 404.2 eV which were attributed to the C-N=C, C-N-C, N-$(C)_3$, and π-excitation that arise due to the generation of amino C-N-H bond, respectively (Figure 3B).[51] Two peaks in the Sn 3d spectrum at 485.6 and 494.2 eV corresponded to Sn $3d_{3/2}$ and Sn $3d_{5/2}$, respectively (Figure 3C). The S 2p spectrum exhibited two peaks at 160.5 and 161.6 eV which corresponded to S $2p_{3/2}$ and S $2p_{1/2}$, respectively, indicating the presence of sulfur anion in SnS_2 (Figure 3D). The Au 4f spectrum exhibited two peaks at 83.1 and 86.7 eV due to the presence of Au $4f_{5/2}$ and Au $4f_{7/2}$, respectively, concluding Au coating on the surface of g-C_3N_4/SnS_2 (Figure 3E). Hence, the aforementioned findings suggest the successful synthesis of g-C_3N_4/SnS_2@Au nanoparticles.

Photothermal Properties, and ROS Detection of g-C_3N_4/SnS_2@Au Nanoparticles

The photothermal properties of the g-C_3N_4/SnS_2@Au nanoparticles were evaluated and are presented in Figure 4A and B. Different concentrations (0.25, 0.5, and 1 mg/mL) of the composite nanoparticles were subjected to NIR laser irradiation (Figure 4A). The temperature of the nanoparticles increased with increasing sample concentration. These nanoparticles exhibited 41 °C temperature at 1 mg/mL concentration. In contrast, the temperature of control group (water) was raised to 25 °C. Thus, the nanoparticles enhanced the PTT effect owing to the presence of a prominent Au nanoparticles as photothermal agent. The photostability of g-C_3N_4/SnS_2@Au nanoparticles was evaluated (Figure 4B). No notable temperature changes were observed after three laser on/off cycles, indicating that these nanoparticles had

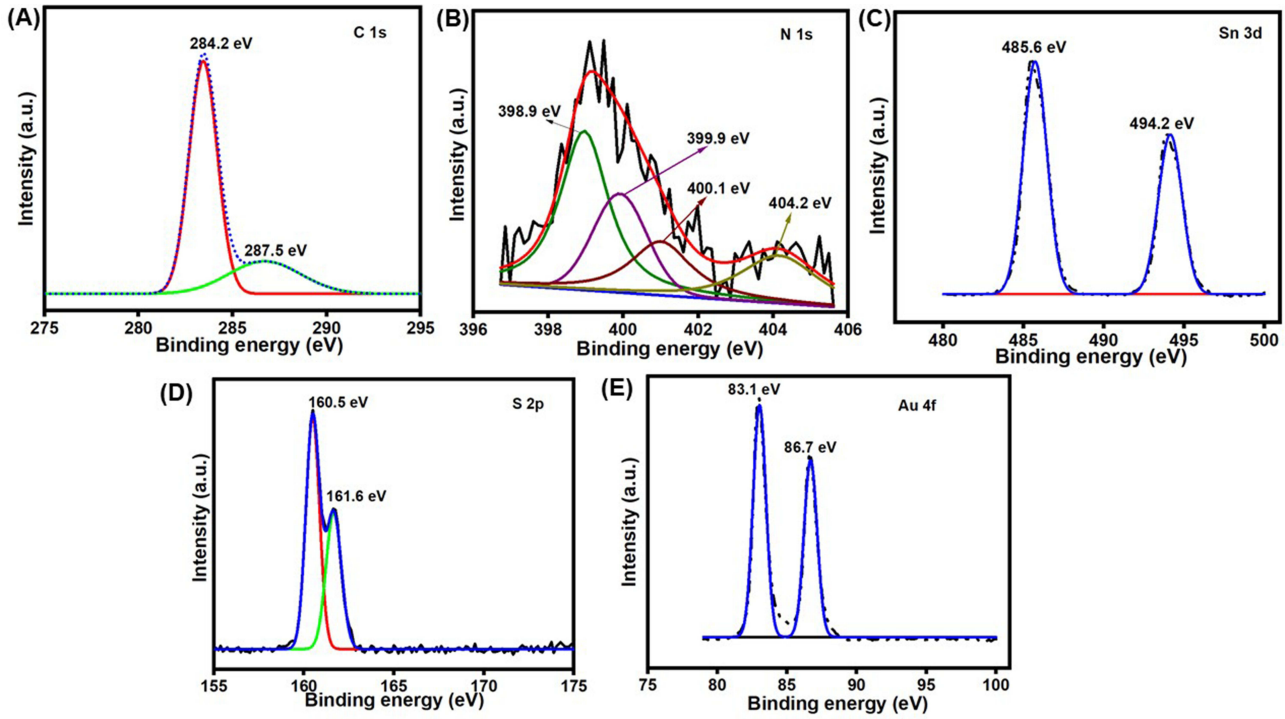

Figure 3 XPS spectra of g-C_3N_4/SnS_2@Au nanoparticles for (**A**) C 1s. (**B**) N 1s. (**C**) Sn 3d. (**D**) S 2p. (**E**) Au 4f.

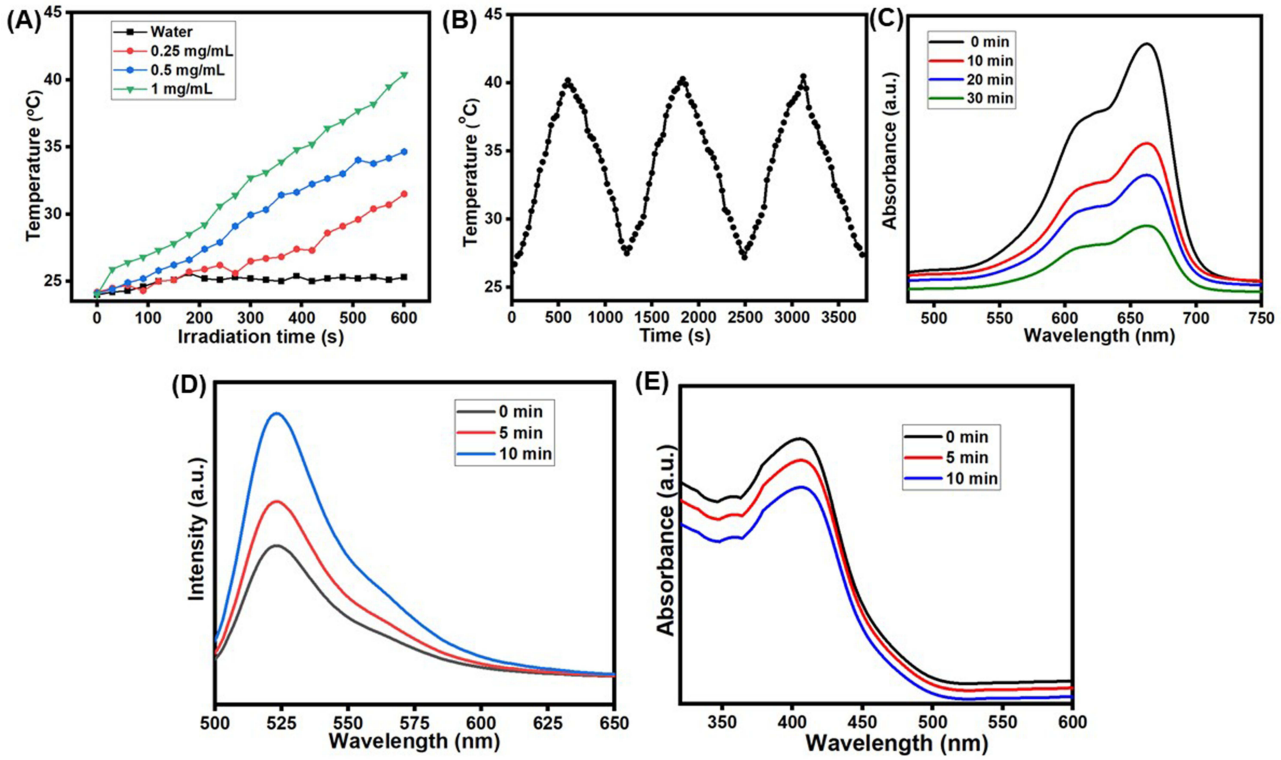

Figure 4 (**A**) The photothermal properties of g-C_3N_4/SnS_2@Au nanoparticles at various concentrations exposed to 808 nm laser. (**B**) The photothermal stability of g-C_3N_4/SnS_2@Au nanoparticles exposed to 808 nm laser over three on/off cycles. (**C**) The MB activity of g-C_3N_4/SnS_2@Au nanoparticles measured at various exposure times. (**D**) ROS detection monitored using DCFH-DA fluorescence spectra treated with different irradiation times of g-C_3N_4/SnS_2@Au nanoparticles (808 nm, 1 W/cm^2). (**E**) Absorbance spectra of DPBF mixed with g-C_3N_4/SnS_2@Au nanoparticles for various laser irradiations.

enhanced photothermal stability. The η value of nanoparticles was 41%, suggesting an excellent photothermal conversion performance. Thus the above findings indicate that these nanoparticles can be utilized as intense photothermal agents to inhibit cancer cells. Hence, these nanoparticles can serve as potent PTT agents for cancer treatment. The degradation activity of the g-C_3N_4/SnS_2@Au nanoparticles was assessed using methylene blue (MB) under laser irradiation. The intensity of the absorption peak at 664 nm for the g-C_3N_4/SnS_2@Au nanoparticles decreased significantly with increasing irradiation time (Figure 4C). After 30 min of laser irradiation, the MB was completely degraded. The above results indicate that the g-C_3N_4/SnS_2@Au nanoparticles can enhance hydroxyl radical ($OH^{\cdot}$) formation under 808 nm laser irradiation, thereby improving photocatalytic activity for ROS generation towards MB degradation. Furthermore, these nanoparticles suggesting that the enhance the electron-hole pair separation and declined the recombination to promote the photocatalytic activity through 808 nm laser irradiation. Thus, these nanoparticles can improve the PDT effect because g-C_3N_4 can be utilized as a promising PS under laser irradiation to induce cancer cell death.[52] ROS formation was monitored using the dichloro-dihydro-fluorescein diacetate (DCFH-DA) fluorescent probe (Figure 4D). The ROS generation ability of the g-C_3N_4/SnS_2@Au nanoparticles was irradiated using an 808 nm laser. The fluorescence intensity of the g-C_3N_4/SnS_2@Au nanoparticles increased continuously with increasing irradiation time due to enhancement of ROS generation with respect to time. Here, ROS generation are responsible in the presence of g-C_3N_4, as an intense photosensitizing agent. These nanoparticles enhanced ROS generation by varying irradiation time. Therefore, g-C_3N_4/SnS_2@Au nanoparticles intensified ROS generation, which can lead to the inhibition of tumor cells by PDT. DPBF served as a ROS probe for investigating singlet oxygen ($^1O_2$). The g-C_3N_4/SnS_2@Au nanoparticle solutions were laser irradiated, as shown in Figure 4E. The absorbance of the sample solution decreased drastically with increasing irradiation time. After 10 min of irradiation, the absorbance intensity of the DPBF solution containing g-C_3N_4/SnS_2@Au nanoparticles with standard characteristic peaks at 410 nm gradually decreased under laser irradiation, suggesting intense

ROS generation due to the g-C_3N_4 used as a photosensitizer.[35] Therefore, these nanoparticles enhanced the PDT effect under laser irradiation, inducing cell apoptosis.

In vitro Synergistic Therapy

The viability of the L929 cells cultured with g-C_3N_4/SnS_2@Au nanoparticles at various concentrations are shown in Figure 5A. Even at a higher concentration (1000 μg/mL), no toxicity was observed in normal cells. The cell viability of g-C_3N_4/SnS_2@Au nanoparticles was greater than 97%, even at higher concentrations. Thus, the g-C_3N_4/SnS_2@Au nanoparticles exhibited good biocompatibility. The cell viability of g-C_3N_4/SnS_2@Au nanoparticles against HepG2 cells irradiated with laser group was decreased as compared to the both control group and unirradiated laser group (Figure 5B). Without laser irradiation group, the cell viability of nanoparticles was over 85%, however with laser irradiation the cell viability was 20%. The HepG2 cells treated with g-C_3N_4/SnS_2@Au nanoparticles under laser irradiation exhibited higher cytotoxicity than the unirradiated and control groups. The cell viability of HepG2 cells treated with g-C_3N_4/SnS_2@Au nanoparticles decreased to 20% under an 808 nm laser owing to synergistic effects of PDT and PTT. The improved PDT and PTT effects occurred due to the intense photosensitizer (g-C_3N_4) and photothermal agent (Au nanoparticles) that can lead to effective cellular apoptosis. Moreover, the intense photosensitizer under exposure to light irradiation produced ROS, which killed the HepG2 cancer cells. As a result, PDT effect occurred.

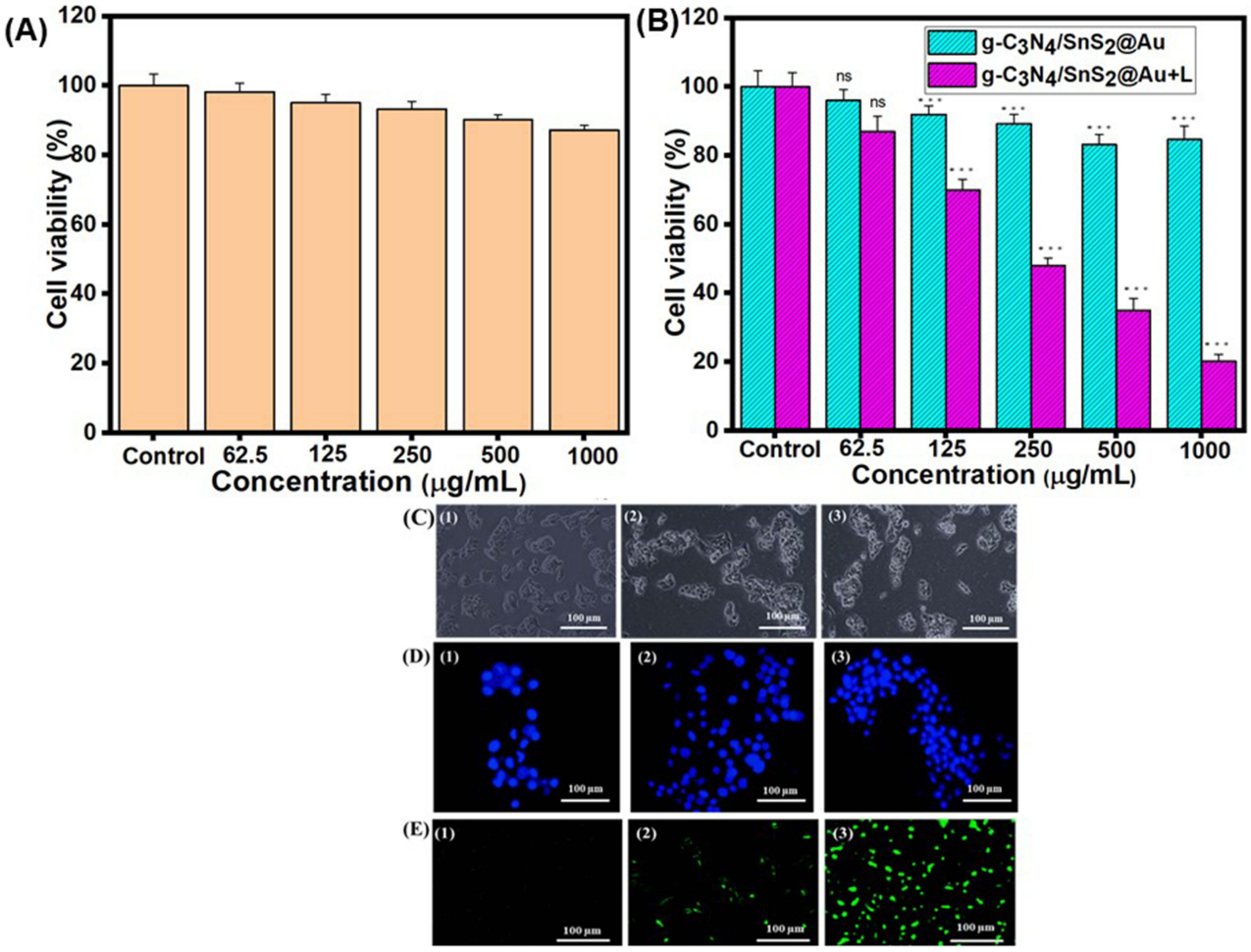

Figure 5 (**A**) Viability of normal fibroblast cells (L929) at different concentrations of g-C_3N_4/SnS_2@Au nanoparticles. (**B**) Cytotoxicity of human liver carcinoma cancer (HepG2) cells treated with g-C_3N_4/SnS_2@Au nanoparticles at various concentrations with or without 808 nm laser irradiation (1 W/cm^2, 5 min). (**C**) Bright field images of HepG2 incubated with g-C_3N_4/SnS_2@Au nanoparticles for various incubation times (1) 0.5 h, (2) 1 h, and (3) 4 h. (**D**) Cellular uptake of HepG2 cells treated with g-C_3N_4/SnS_2@Au stained with DAPI for different incubation times (1) 0.5 h, (2) 1 h, and (3) 4 h. (**E**) Fluorescence images of HepG2 cells stained with DCFH-DA (1) control, (2) g-C_3N_4/SnS_2@Au, and (3) g-C_3N_4/SnS_2@Au nanoparticles with 808 nm laser irradiation (*** denote $p < 0.001$ and ns denotes no significant difference).

Light absorption converts optical energy into heat energy using the photothermal agent, resulting in cancer cell death to prompt the improved PPT effect. Hence, the concurrent treatment of PDT and CDT can lead to intensified cellular damage as compared to monotherapy treatment. Therefore, g-C_3N_4/SnS_2@Au nanoparticles with laser treatment exhibited higher cellular apoptosis due to a synergistic therapeutic effect. Therefore, these nanoparticles possess intense therapeutic efficiency and can induce 80% cell apoptosis through combinational therapeutic effects for cancer treatment. The cellular uptake behavior of the g-C_3N_4/SnS_2@Au nanoparticles was investigated using fluorescence microscopy (Figure 5C). HepG2 cells incubated with g-C_3N_4/SnS_2@Au nanoparticles for various incubation times were observed. These nanoparticles can be effectively internalized into cells through endocytosis. Therefore, these nanoparticles possessed higher cellular uptake, which could be beneficial for intense therapeutic applications. Furthermore, ICP-MS technique was used to measure the internalized quantities of g-C_3N_4/SnS_2@Au nanoparticles for HepG2 cells under various incubation time intervals (1 h and 4 h) and resultant data presented in Figure S4. The uptake amount of Au in HepG2 cells is significantly increased with increase in the incubation time period. This suggests that the variable incubation times can allow g-C_3N_4/SnS_2@Au nanoparticles to penetrate HepG2 cells. The g-C_3N_4/SnS_2@Au nanoparticles possessed three times higher cellular uptake for 4 h as compared to the 1h incubation time period. The above results proved that, the g-C_3N_4/SnS_2@Au nanoparticles possessed higher cellular uptake which can effectively internalized in the cells through endocytosis. Furthermore, the HepG2 cells were stained with DAPI that can binds to cell nuclei (Figure 5D). It exhibited a weak blue fluorescence signal at 0.5 h incubation. Blue fluorescence intensity gradually and consistently increased with increasing incubation time. Thus with an increase in incubation time, these nanoparticles showed intense blue fluorescence, which could bind directly to nuclei and obstruct DNA replication. Hence, these nanoparticles can induce cellular apoptosis through an intense therapeutic effect. ROS generation was examined using DCFH-DA as a fluorescent probe in cells, which could liberate DCF products and enhance green fluorescence emission. HepG2 cells treated with g-C_3N_4/SnS_2@Au nanoparticles via NIR laser irradiation exhibited an intense green fluorescence signal, as shown in Figure 5E. Conversely, g-C_3N_4/SnS_2@Au nanoparticles exhibited weak fluorescence signals similar to those of the control groups. The laser-induced cytotoxicity of g-C_3N_4/SnS_2@Au nanoparticles generated efficient ROS production that resulting the PDT therapeutic efficacy. Thus, g-C_3N_4/SnS_2@Au nanoparticles under laser irradiation generated intensify ROS generation as g-C_3N_4 acts as a suitable PS. Therefore, these nanoparticles exhibit an improved PDT effect that can inhibit cancer cells.

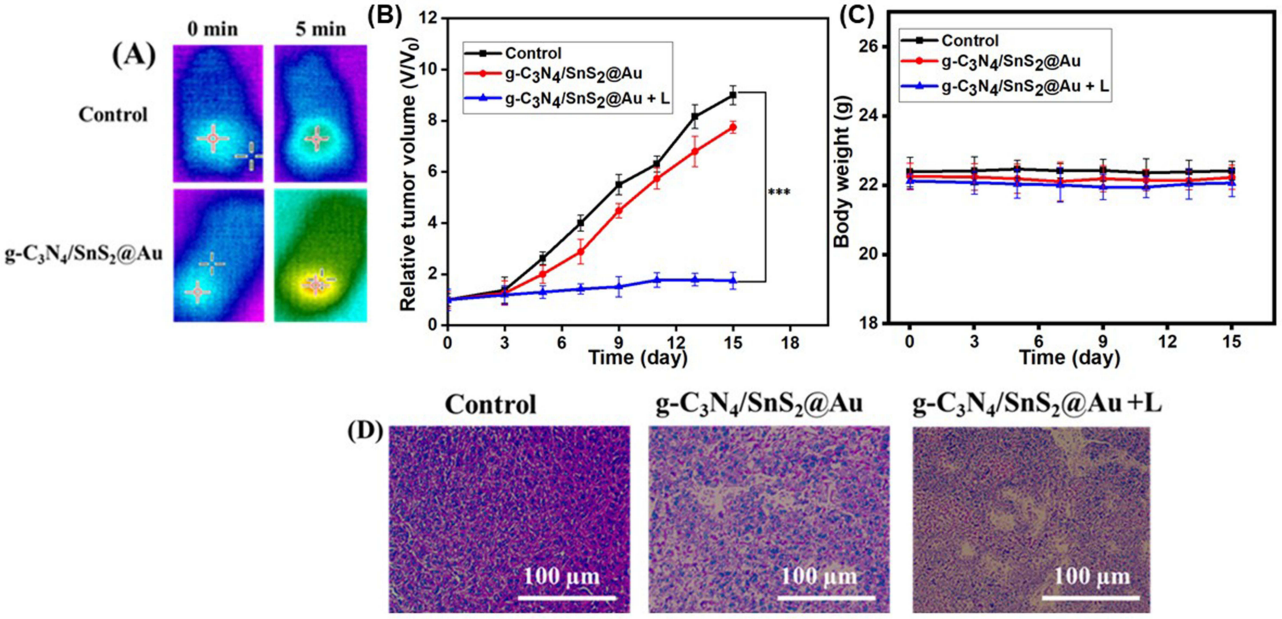

Figure 6 (**A**) Infrared imaging of tumor-bearing mice for control and g-C_3N_4/SnS_2@Au nanoparticles subjected with an 808 nm laser. (**B**) Tumor volume and (**C**) body weight analysis of mice with different treatment groups control, g-C_3N_4/SnS_2@Au and g-C_3N_4/SnS_2@Au under 808 nm laser irradiation. (**D**) H&E staining images of tumor after various treatment groups control, g-C_3N_4/SnS_2@Au and g-C_3N_4/SnS_2@Au with irradiation of 808 nm laser (*** denote $p < 0.001$, scale bar = 100 μm).

In vivo Antitumor Effect

The antitumor effects of nanoparticles were evaluated in HepG2 tumor-bearing mice. The g-C_3N_4/SnS_2@Au nanoparticles were intratumorally injected into mice. The tumor temperature was measured using an infrared thermal imaging camera. The tumor site temperature of g-C_3N_4/SnS_2@Au nanoparticles was raised to 42.9°C compared to the control group (36.3°C) after 5 min laser irradiation (Figure 6A). These findings suggest that the g-C_3N_4/SnS_2@Au nanoparticles exhibit an enhanced PTT effect in vivo which can damage tumor cells. The tumor volume of g-C_3N_4/SnS_2@Au nanoparticles under laser irradiation exhibited an intense tumor ablation effect. Conversely, the control and non-irradiated groups showed no remarkable tumor inhibitory effects (Figure 6B). The body weights of the mice did not change during the treatment period, indicating that there were no side effects of the g-C_3N_4/SnS_2@Au nanoparticles (Figure 6C). Therefore, g-C_3N_4/SnS_2@Au nanoparticles with 808 nm laser irradiation possessed superior antitumor effects owing to the combined PDT and PTT effects. The g-C_3N_4/SnS_2@Au nanoparticles group treated under irradiation of NIR laser demonstrated intense tumor growth suppression as compared to control group as represented digital photograph images of mice bearing tumors (Figure S5A and B). Figure 6D shows the hematoxylin and eosin (H&E)-stained images of the tumor tissue for various treatment groups. The g-C_3N_4/SnS_2@Au nanoparticles under laser irradiation group showed severe tumor cell apoptosis as compared to the non-irradiated g-C_3N_4/SnS_2@Au nanoparticle group, whereas no obvious damaged tumor cells were found in the control. Hence, the above results demonstrated that these nanoparticles exhibit superior anticancer effects with an 808 nm laser by a combination of therapeutic effects.

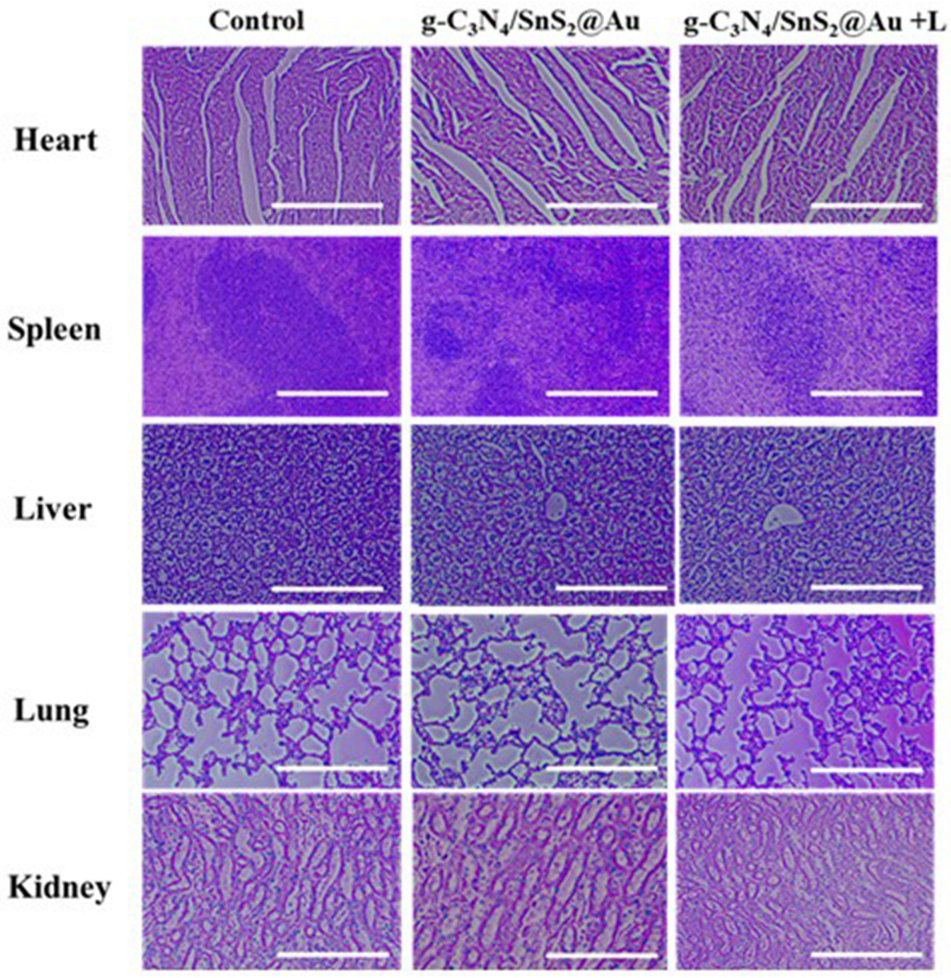

Figure 7 H&E-stained images of the main organs from various treatment groups (scale bar = 100 μm).

H&E-stained images of the main organs are shown in Figure 7. As shown in Figure 7, no abnormal inflammation was observed after 14 days of treatment. Thus, these nanoparticles possessed good biocompatibility and enhanced antitumor efficiency through synergistic therapeutic PDT and PTT effects.

Conclusions

In summary, g-C_3N_4/SnS_2@Au nanoparticles were successfully developed. The synthesized photocatalytic heterostructure nanomaterials exhibited high efficiency for photogenerated charge carrier separation and improved enhanced photocatalytic activity performance. The nanoparticles exhibited enhanced ROS formation by PDT pathways (Type-I and Type-II) through irradiation with an NIR laser because of the promising PS, g-C_3N_4. Moreover, these nanoparticles exhibited an intense PTT effect, which was derived from the Au nanoparticles through NIR laser irradiation. Both in vitro and in vivo results indicated that the g-C_3N_4/SnS_2@Au nanoparticles exhibited high biocompatibility, efficient cancer cell apoptosis, and excellent tumor inhibition through synergistic PDT and PTT effects. The results proved that these nanoparticles have great potential as a combinatorial effect under 808 nm laser irradiation for cancer treatment.

Acknowledgments

The authors are grateful for the financial support provided by the National Science and Technology Council of Taiwan (NSTC 112-2221-E-027-038-MY3). We also would like to acknowledge the technical assistance from the Precision Analysis and Material Research Center of the National Taipei University of Technology (Taipei Tech).

Disclosure

The authors declare no known competing financial interests or personal relationships that could have influenced the work reported in this paper.

References

1. Luo M, Yukawa H, Sato K, et al. Multifunctional magnetic CuS/Gd_2O_3 nanoparticles for fluorescence/magnetic resonance bimodal imaging-guided Photothermal-intensified Chemodynamic synergetic therapy of targeted tumors. *ACS Appl Mater Interfaces*. 2022;14(30):34365–34376. doi:10.1021/acsami.2c06503
2. Zhang Q, Sun S, Wang Z, et al. Dandelion-inspired hierarchical upconversion nanoplatform for synergistic chemo-photodynamic therapy in vitro. *ACS Appl Bio Mater*. 2020;3(9):6015–6024. doi:10.1021/acsabm.0c00645
3. Dash P, Panda PK, Su C, et al. Near-infrared-driven upconversion nanoparticles with photocatalysts through water-splitting towards cancer treatment. *J Mater Chem B*. 2024;12(16):3881–3907. doi:10.1039/D3TB01066J
4. Qi Y, Ye J, Ren S, et al. Temperature Feedback-Controlled Photothermal/Photodynamic/Chemodynamic Combination Cancer Therapy Based on $NaGdF_4$: er, Yb@ $NaGdF_4$:Nd@Cu-BIF Nanoassemblies. *Adv Healthc Mater*. 2020;9(21):2001205. doi:10.1002/adhm.202001205
5. Dash P, Thirumurugan S, Tseng CL, et al. Synthesis of Methotrexate-Loaded Dumbbell-Shaped Titanium Dioxide/Gold Nanorods Coated with Mesoporous Silica and Decorated with Upconversion Nanoparticles for Near-Infrared-Driven Trimodal Cancer Treatment. *ACS Appl Mater Interfaces*. 2023;15(28):33335–33347. doi:10.1021/acsami.3c04300
6. Sheng Y, Ren Q, Tao C, et al. Construction of PEGylated chlorin e6@CuS-Pt theranostic nanoplatforms for nanozymes-enhanced photodynamic-photothermal therapy. *J Colloid Interface Sci*. 2023;645:122–132. doi:10.1016/j.jcis.2023.04.092
7. Yin Y, Gao L, Sun P, et al. pH/ROS dual stimuli-responsive anionic flexible supramolecular organic frameworks for synergistic therapy. *Acta Biomater*. 2023;172:395–406. doi:10.1016/j.actbio.2023.10.019
8. Zhang J, Wang N, Li Q, et al. A two-pronged photodynamic nanodrug to prevent metastasis of basal-like breast cancer. *Chem Commun*. 2021;57(18):2305–2308. doi:10.1039/D0CC08162K
9. Ma J, Tai Z, Li Y, et al. Dissolving Microneedle-Based Cascade-Activation Nanoplatform for Enhanced Photodynamic Therapy of Skin Cancer. *Int J Nanomed*. 2024;19:2057–2070. doi:10.2147/IJN.S443835
10. Zhang Y, Zhu X, Zhang J, et al. Synergistic upconversion photodynamic and photothermal therapy under cold near-infrared excitation. *J Colloid Interface Sci*. 2021;600:513–529. doi:10.1016/j.jcis.2021.05.017
11. Xu M, Yang G, Bi H, et al. Combination of CuS and g-C_3N_4 QDs on upconversion nanoparticles for targeted photothermal and photodynamic cancer therapy. *Chem Eng J*. 2019;360:866–878. doi:10.1016/j.cej.2018.12.052
12. Yang C, Chang M, Yuan M, et al. NIR-Triggered Multi-Mode Antitumor Therapy Based on Bi_2Se_3/Au Heterostructure with Enhanced Efficacy. *Small*. 2021;17(28):2100961. doi:10.1002/smll.202100961
13. Aggarwal V, Tuli HS, Varol A, et al. Role of reactive oxygen species in cancer progression: molecular mechanisms and recent advancements. *Biomolecules*. 2019;9(11):735. doi:10.3390/biom9110735
14. Shi Z, Zhang K, Zada S, et al. Upconversion nanoparticle-induced multimode photodynamic therapy based on a metal–organic framework/titanium dioxide nanocomposite. *ACS Appl Mater Interfaces*. 2020;12(11):12600–12608. doi:10.1021/acsami.0c01467
15. Zhong Y, Zhang X, Yang L, et al. Hierarchical dual-responsive cleavable nanosystem for synergetic photodynamic/photothermal therapy against melanoma. *Mater Sci Eng C*. 2021;131:112524. doi:10.1016/j.msec.2021.112524

16. Dou J, Bian W, Zheng X, et al. A ZIF-based drug delivery system as three-in-one platform for joint cancer therapy. *Mater Chem Phys*. 2023;297:127345. doi:10.1016/j.matchemphys.2023.127345
17. Du K, Zhao S, Feng J, et al. Engineering $Cu_{2-x}S$-conjugated upconverting nanocomposites for NIR-II light-induced enhanced chemodynamic/photothermal therapy of cancer. *J Mater Chem B*. 2021;9(35):7216–7228. doi:10.1039/D1TB00337B
18. Wang Y, Niu N, Huang Y, et al. Three-Pronged Attack by Hybrid Nanoplatform Involving MXenes, Upconversion Nanoparticle and Aggregation-Induced Emission Photosensitizer for Potent Cancer Theranostics. *Small Methods*. 2022;6(8):2200393. doi:10.1002/smtd.202200393
19. Tian Y, Ding Z, Zheng X, et al. Porphyrin-based porous organic polymer coated ZIF-8 nanoparticles as tumor targeted photosensitizer for combination cancer photodynamic/photothermal therapy. *Micropor Mesopor Mater*. 2023;355:112562. doi:10.1016/j.micromeso.2023.112562
20. Liu H, Zhang J, Jia Y, et al. Theranostic nanomotors for tumor multimode imaging and photothermal/photodynamic synergistic therapy. *Chem Eng J*. 2022;442:135994. doi:10.1016/j.cej.2022.135994
21. Cai L, Dong L, Sha X, et al. Exfoliation and in situ functionalization of MoS_2 nanosheets for MRI-guided combined low-temperature photothermal therapy and chemotherapy. *Mater Des*. 2021;210:110020. doi:10.1016/j.matdes.2021.110020
22. Zhou G, Wang YS, Jin Z, et al. Porphyrin–palladium hydride MOF nanoparticles for tumor-targeting photoacoustic imaging-guided hydrogenothermal cancer therapy. *Nanoscale Horiz*. 2019;4(5):1185–1193. doi:10.1039/C9NH00021F
23. Xu Y, Fan M, Yang W, et al. Homogeneous carbon/potassium-incorporation strategy for synthesizing red polymeric carbon nitride capable of near-infrared photocatalytic H_2 production. *Adv Mater*. 2021;33(39):2101455. doi:10.1002/adma.202101455
24. Chen T, Yao T, Peng H, et al. An injectable hydrogel for simultaneous photothermal therapy and photodynamic therapy with ultrahigh efficiency based on carbon dots and modified cellulose nanocrystals. *Adv Funct Mater*. 2021;31(45):2106079. doi:10.1002/adfm.202106079
25. Xu J, Han W, Yang P, et al. Tumor microenvironment-responsive mesoporous MnO_2-coated upconversion nanoplatform for self-enhanced tumor theranostics. *Adv Funct Mater*. 2018;28(36):1803804. doi:10.1002/adfm.201803804
26. Wang X, Xu J, Yang D, et al. Fe_3O_4@ MIL-100 (Fe)-UCNPs heterojunction photosensitizer: rational design and application in near infrared light mediated hypoxic tumor therapy. *Chem Eng J*. 2018;354:1141–1152. doi:10.1016/j.cej.2018.08.070
27. Zhang C, Chen WH, Liu LH, et al. An O_2 self-supplementing and reactive-oxygen-species-circulating amplified nanoplatform via H_2O/H_2O_2 splitting for tumor imaging and photodynamic therapy. *Adv Funct Mater*. 2017;27(43):1700626. doi:10.1002/adfm.201700626
28. Zhang Y, Cheng Y, Yang F, et al. Near-infrared triggered $Ti_3C_2/g\text{-}C_3N_4$ heterostructure for mitochondria-targeting multimode photodynamic therapy combined photothermal therapy. *Nano Today*. 2020;34:100919. doi:10.1016/j.nantod.2020.100919
29. Liu E, Chen J, Ma Y, et al. Fabrication of 2D $SnS_2/g\text{-}C_3N_4$ heterojunction with enhanced H_2 evolution during photocatalytic water splitting. *J Colloid Interface Sci*. 2018;524:313–324. doi:10.1016/j.jcis.2018.04.038
30. Dai J, Song J, Qiu Y, et al. Gold nanoparticle-decorated $g\text{-}C_3N_4$ nanosheets for controlled generation of reactive oxygen species upon 670 nm laser illumination. *ACS Appl Mater Interfaces*. 2019;11(11):10589–10596. doi:10.1021/acsami.9b01307
31. Patra R, Panda PK, Lin TH, et al. Graphitic carbon nitride nanosheet and ferroelectric $PbTiO_3$ nanoplates S-scheme heterostructure for enhancing hydrogen production and textile dye degradation. *Chem Eng Sci*. 2024;295:120133. doi:10.1016/j.ces.2024.120133
32. Patra R, Dash P, Panda PK, Yang PC. A Breakthrough in Photocatalytic Wastewater Treatment: the Incredible Potential of $g\text{-}C_3N_4$/Titanate Perovskite-Based Nanocomposites. *Nanomaterials*. 2023;13(15):2173. doi:10.3390/nano13152173
33. Feng L, He F, Liu B, et al. $g\text{-}C_3N_4$ coated upconversion nanoparticles for 808 nm near-infrared light triggered phototherapy and multiple imaging. *Chem Mater*. 2016;28(21):7935–7946. doi:10.1021/acs.chemmater.6b03598
34. Qian G, Wen T, Shuai Y, et al. Photothermal and photodynamic effects of $g\text{-}C_3N_4$ nanosheet/Bi_2S_3 nanorod composites with antibacterial activity for tracheal injury repair. *ACS Appl Nano Mater*. 2022;5(11):16528–16543. doi:10.1021/acsanm.2c03569
35. Yang D, Yang G, Gai S, et al. Multifunctional theranostics for dual-modal photodynamic synergistic therapy via stepwise water splitting. *ACS Appl Mater Interfaces*. 2017;9(8):6829–6838. doi:10.1021/acsami.6b15203
36. Chen L, Chen M, Jiang D, Xie J. A facile strategy for $SnS_2/g\text{-}C_3N_4$ heterojunction composite and the mechanism in photocatalytic degradation of MO. *J Mol Catal a Chem*. 2016;425:174–182. doi:10.1016/j.molcata.2016.10.003
37. Samanta S, Martha S, Parida K. Facile synthesis of $Au/g\text{-}C_3N_4$ nanocomposites: an inorganic/organic hybrid plasmonic photocatalyst with enhanced hydrogen gas evolution under visible-light irradiation. *ChemCatChem*. 2014;6(5):1453–1462. doi:10.1002/cctc.201300949
38. Zhang R, Bi L, Wang D, et al. Investigation on various photo-generated carrier transfer processes of $SnS_2/g\text{-}C_3N_4$ heterojunction photocatalysts for hydrogen evolution. *J Colloid Interface Sci*. 2020;578:431–440. doi:10.1016/j.jcis.2020.04.033
39. Parveen N, Ansari SA, Alamri HR, et al. Facile synthesis of SnS_2 nanostructures with different morphologies for high-performance supercapacitor applications. *ACS omega*. 2018;3(2):1581–1588. doi:10.1021/acsomega.7b01939
40. Panda AK, Murugan K, Sakthivel R, et al. A non-enzymatic, biocompatible electrochemical sensor based on N-doped graphene quantum dot-incorporated SnS_2 nanosheets for in situ monitoring of hydrogen peroxide in breast cancer cells. *Colloids Surf B*. 2023;222:113033. doi:10.1016/j.colsurfb.2022.113033
41. Di T, Zhu B, Cheng B, Yu J, Xu J. A direct Z-scheme $g\text{-}C_3N_4/SnS_2$ photocatalyst with superior visible-light CO_2 reduction performance. *J Catal*. 2017;352:532–541. doi:10.1016/j.jcat.2017.06.006
42. Huang N, Liu J, Gan L, Long M. Preparation of size-tunable SnS_2 nanocrystals in situ adjusted by nanoporous graphitic carbon nitride in the process of hydrothermal synthesis with enhanced photocatalytic performance. *Mater Lett*. 2017;195:224–227. doi:10.1016/j.matlet.2017.02.131
43. Yang J, Sun L, Hui S, et al. Ag functionalized SnS_2 with enhanced photothermal activity for safe and efficient wound disinfection. *Biomater Sci*. 2021;9(13):4728–4736. doi:10.1039/D1BM00429H
44. Zhang Y, Hu L, Zhou H, et al. NIR photothermal-enhanced electrocatalytic and photoelectrocatalytic hydrogen evolution by polyaniline/SnS_2 nanocomposites. *ACS Appl Nano Mater*. 2022;5(1):391–400. doi:10.1021/acsanm.1c03211
45. Soleimany A, Khoee S, Dias S, Sarmento B. Exploring low-power single-pulsed laser-triggered two-photon photodynamic/photothermal combination therapy using a gold nanostar/graphene quantum dot nanohybrid. *ACS Appl Mater Interfaces*. 2023;15(17):20811–20821. doi:10.1021/acsami.3c03578
46. Pawar RC, Kang S, Ahn SH, Lee CS. Gold nanoparticle modified graphitic carbon nitride/multi-walled carbon nanotube ($g\text{-}C_3N_4$/CNTs/Au) hybrid photocatalysts for effective water splitting and degradation. *RSC Adv*. 2015;5(31):24281–24292. doi:10.1039/C4RA15560B
47. Deng X, Liang S, Cai X, et al. Yolk–shell structured Au nanostar@ metal–organic framework for synergistic chemo-photothermal therapy in the second near-infrared window. *Nano Lett*. 2019;19(10):6772–6780. doi:10.1021/acs.nanolett.9b01716

48. Pan L, Liu J, Shi J. Nuclear-targeting gold nanorods for extremely low NIR activated photothermal therapy. *ACS Appl Mater Interfaces*. 2017;9(19):15952–15961. doi:10.1021/acsami.7b03017
49. Subramanyam P, Vinodkumar T, Deepa M, Subrahmanyam C. Gold nanoparticle decorated bismuth sulfide nanorods for enhanced photoelectrochemical hydrogen production. *J Mater Chem C*. 2019;7(21):6398–6405. doi:10.1039/C9TC00759H
50. Wen P, Sun Y, Li H, et al. A highly active three-dimensional Z-scheme ZnO/Au/g-C_3N_4 photocathode for efficient photoelectrochemical water splitting. *Appl Catal B*. 2020;263:118180. doi:10.1016/j.apcatb.2019.118180
51. Faisal M, Jalalah M, Harraz FA, et al. Au nanoparticles-doped g-C_3N_4 nanocomposites for enhanced photocatalytic performance under visible light illumination. *Ceram Int*. 2020;46(14):22090–22101. doi:10.1016/j.ceramint.2020.05.250
52. Lin LS, Cong ZX, Li J, et al. Graphitic-phase C_3N_4 nanosheets as efficient photosensitizers and pH-responsive drug nanocarriers for cancer imaging and therapy. *J Mater Chem B*. 2014;2(8):1031–1037. doi:10.1039/c3tb21479f